Original Paper

Eletrônica de Potência
Open Journal of Power Electronics

Received July 30, 2025; Received in revised form November 06, 2025, December 10, 2025; Accepted January 05, 2026; Date of publication January 20, 2026.
The review of this paper was arranged by Associate Editor Montiê A. Vitorino and Editor-in-Chief Allan F. Cupertino.
Digital Object Identifier http://doi.org/10.18618/REP.e202607

Design Methodology for Coupled Inductors Aimed at Reducing Leakage Inductance, Proximity Effect, and Electromagnetic Interference in Quasi-Resonant Flyback LED Drivers

João R. C. Amado[1,*], Kalyl S. A. Ali[1], Giulia K. Grassi[1], Hentony A. Lobo[1], Renan R. Duarte[1], Marco A. D. Costa[1]

[1]Federal University of Santa Maria, Gedre - Intelligence in Lighting, Santa Maria, RS, Brazil.

e-mail: joaorenatoamado@hotmail.com*, kalyl-sinhorini.ali@acad.ufsm.br, giulia.grassi@acad.ufsm.br, hentony.lobo@gmail.com, renan.duarte@gedre.ufsm.br, marcodc@gedre.ufsm.br.
*Corresponding author.

ABSTRACT This paper presents a comprehensive study on the influence of winding geometry on leakage inductance and proximity effect losses in coupled inductors applied to quasi-resonant flyback converters for LED drivers. Eleven coupled inductors were designed using the same PQ3220 core, varying the number of layers, interleaving level, and wiring geometry to evaluate their impact on performance. The leakage inductance of each inductor was calculated analytically and measured experimentally, showing strong correlation and validating the analytical method. Additionally, proximity effect losses were estimated through simulations based on winding temperature measurements, allowing the extraction of the AC resistance and proximity factor for each design. The experimental setup involved a 60 W quasi-resonant flyback LED driver operating at around 50 V output, where voltage spikes on the MOSFET, system efficiency, and critical component temperatures were analyzed. Results show that increasing the interleaving level significantly reduces leakage inductance, proximity losses, and electromagnetic emissions, leading to improved efficiency, lower thermal stress, and facilitated regulatory compliance. This study highlights the importance of magnetic design in achieving high-performance LED drivers and provides practical guidelines for minimizing parasitic effects in coupled inductors without increasing component count.

KEYWORDS Coupled inductor, flyback, leakage inductance, LED driver, proximity effect.

I. INTRODUCTION

Compared to other lighting technologies, Light Emitting Diodes (LEDs) offer several advantages such as long lifespan, higher efficacy, robustness, and reliability, among other features [2]. To fully benefit from their efficiency and longevity, LEDs must be powered by current-controlled switched mode converters [3].

Switched-mode converters are devices that convert input voltages and currents to stable and appropriate output levels according to the load requirements. For power levels up to 150 W, the flyback topology is one of the most widely used, as it features a low number of components and provides isolation between input and output through a coupled inductor [4].

One drawback of the flyback topology is its relatively high switching losses. However, with the introduction of the control method for a quasi-resonant flyback converter (QR), the switching losses of the main switch are significantly reduced, leading to an increase in the overall efficiency of the converter [5]. Other limitations of the flyback converter include dissipative losses in the snubber circuit and high voltage stress on the main switch during turn-off events [5]. This last issue is mainly caused by the leakage inductance present in the coupled inductor. The energy stored in this parasitic inductance results in voltage spikes, which become more severe as the converter power increases [6].

Leakage inductance behavior itself has also been analyzed in various contexts. High-frequency models such as [7] show that leakage inductance decreases with frequency due to eddy currents redistribution and compare several interleaving arrangements at MHz range operation, whereas [8] examines how proximity induced currents, air gap placement, and layer distribution affect AC resistance in flyback transformers, concluding that interleaving benefits are more limited in flyback structures than in forward types. Other works have demonstrated lakage reduction concepts through geometric modification of the winding layout [9], though typically evaluating only a single magnetic structure without systematically varying interleaving level or window utilization.

Circuit level attempts to mitigate the adverse effects of leakage inductance have also been proposed, including active clamping techniques [5], lossless snubbers [10], [11] and twin-pulse clamp control strategies [12], that demonstrate effective recovery of leakage energy and reduced switching stress at the expense of increased circuit complexity, requiring additional components and interconnections, which can increase cost and reduce power density [6], [10], [11] Similarly, the EMI implications of leakage inductance were explored in [13], which shows that higher leakage inductance increases high-frequency emissions and voltage spikes, although the analysis relies on artificially modifying leakage in a simplified equivalent circuit rather than investigating its magnetic origin or evaluating different winding arrangements.

Previous analytical studies have also extensively investigated the mechanisms of copper loss in flyback magnetics, such as [14], which derives closed form expressions for AC resistance based on equivalent permeability and multilayer field approximations, and [15], which extends these formulations through fast and accurate prediction of skin and proximity effect losses using methods with finite element analysis validation. More recent developments, including [16] and [17], propose improved analytical models for evaluating high-frequency winding losses in interleaved and non-interleaved structures, while works such as [18], [19], and [20] provide broader optimization frameworks that account for core losses, AC and DC resistance, fringing, and geometric constraints. Although these studies offer valuable tools for estimating magnetic losses, their focus remains primarily on analytical modeling or on the evaluation of a limited number of prototypes, without experimentally examining how different winding geometries influence leakage inductance or propagate to converter level characteristics such as voltage stress, snubber dissipation, thermal behavior, efficiency, and conducted EMI.

Despite these important contributions, the existing literature generally treats leakage inductance estimation, AC loss modeling, winding optimization, EMI behavior, and snubber stress as largely independent topics. Therefore, this paper investigates the application of different winding techniques to reduce leakage inductance in coupled inductors and evaluates their impact on the performance of a quasi-resonant flyback LED driver. Expanding upon the preliminary results presented in [1], the present work provides a more comprehensive analysis by incorporating proximity effect estimation for each implemented prototype, detailed thermal characterization, and conducted EMI measurements. In addition, this work contributes to the literature by experimentally demonstrating how analytical leakage inductance formulations, derived from classical multilayer winding theory, translate into measurable performance improvements in a practical converter. The study systematically implements and compares eleven coupled inductor prototypes, all designed using the same analytical framework and evaluated under identical operating conditions, to assess how geometric parameters such as interleaving level, layer distribution, and turns ratio affect converter-level behavior. These prototypes were developed on the same PQ core, enabling controlled comparisons of leakage inductance, AC resistance and losses, thermal performance, efficiency, snubber losses, MOSFET voltage stress, and conducted EMI. The results show that optimized winding arrangements, particularly those improving magnetic coupling, lead to significant reductions in leakage inductance and AC losses, which in turn translate into measurable improvements in converter behavior, including lower voltage stress, reduced snubber dissipation, improved efficiency, and enhanced EMI compliance. These findings provide practical guidelines and quantitative insights that help bridge the gap between theoretical formulations and the constraints of low-cost, mass-produced magnetic components used in LED driver applications.

This work is organized as follows: Section II presents an overview of the operation of the quasi-resonant flyback converter. Section III discusses the flyback coupled inductors, as well as the origin of leakage inductance and its impacts on converter performance, and high-frequency effects such as skin and proximity effects are analyzed, as they contribute significantly to increased AC resistance and copper losses in high-frequency magnetic components. Section V describes the design and implementation of eleven coupled inductors with different interleaving topologies. Section VI presents experimental results obtained from a quasi-resonant flyback converter using the implemented inductors, with emphasis on efficiency, voltage stress, and temperature measurements, and analyzes the impact of leakage inductance reduction on converter performance. Also in Section VI, a detailed analysis of proximity effect losses in the implemented inductors, supported by thermal measurements and FEM simulations, is provided. The last results presented in Section VI address the impacts of leakage inductance reduction on electromagnetic interference and compliance. Finally, conclusions are summarized in Section VII.

II. QUASI-RESONANT FLYBACK CONVERTER

The quasi-resonant operating mode in flyback converters represents a significant advancement over conventional flyback designs. These converters use valley switching, where the power switch is turned on when the voltage across it reaches a minimum. This reduces switching losses and improves overall system efficiency, reduces electromagnetic noise generated by the converter, and reduces thermal stress on the components, thereby extending the lifespan of the power converter [21]–[23].

The quasi-resonant flyback converter operates by adjusting the switching frequency so that the power switch is turned on when the drain-to-source voltage of the transistor reaches a minimum after the demagnetization of the coupled inductor. This voltage valley occurs naturally due to the interaction

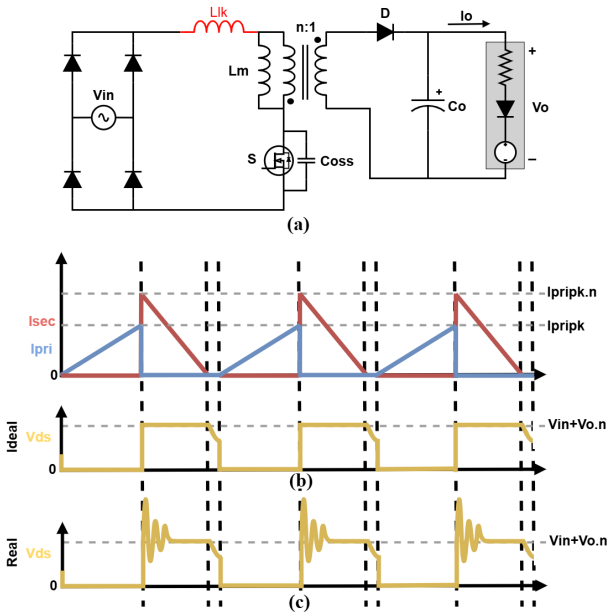

FIGURE 1. Topology of a quasi-resonant flyback converter highlighting the main components and the leakage inductance (a), ideal drain-to-source voltage waveform (b), and drain-to-source voltage waveforms accounting leakage inductance effects (c).

between the primary inductance of the transformer and the parasitic capacitance of the circuit [5].

The typical operational sequence of a quasi-resonant flyback converter includes three stages. During the first stage, the switch is on and current flows through the primary winding of the coupled inductor, storing energy in the magnetic field. During the second stage, the switch is turned off, and the energy stored in the magnetic field is transferred to the secondary winding, supplying the load. After the energy is fully transferred, a voltage oscillation appears across the drain-to-source terminals of the switch due to the resonance between the transformer's primary inductance and other circuit elements, such as the switch output capacitance. The switch is turned on again when this oscillation reaches its minimum point (valley) [24], [25].

Fig. 1 shows the topology of a quasi-resonant flyback converter, highlighting the main components and the leakage inductance (a), as well as the ideal drain-to-source voltage waveform of the switch (b).

III. FLYBACK COUPLED INDUCTORS

Often referred to as a transformer, the magnetic element in the flyback converter is, in fact, a coupled inductor with multiple windings [26]. Coupled inductors are inductors that share part of their magnetic flux lines through a common core. Depending on the design and application, a coupled inductor can store energy, as is the case in the flyback converter. This energy storage occurs in the air gap of the core, which may be discrete or distributed [27].

Each winding of the coupled inductor functions as an inductor on its own, at one or more moments during the operation of the circuit in which it is used. In the case of the flyback converter, for instance, the primary winding operates as an inductor when magnetized during the conduction period of the main switch, while the secondary winding acts as an inductor during demagnetization, transferring energy to the load when the main switch is open [27], [28]. Magnetic coupling in coupled inductors results in fluxes generated with the same polarity, which add up and store energy in the core. This is not the case for transformers, where the fluxes cancel each other and the net flux in the core is negligible [27].

Among the advantages of using coupled inductors are the possibility of large voltage transformations and the provision of isolation between windings. However, inherent characteristics such as leakage inductance and proximity effect must be taken into account during the design of the magnetic element [26], [27].

A. LEAKAGE INDUCTANCE AND ITS EFFECTS

Leakage inductance is an inherent phenomenon in coupled inductors and transformers, being more pronounced in the former. It refers to the amount of magnetic flux that is not transferred between the windings of the magnetic element [29]. In flyback converters, this phenomenon results in undesired energy being stored in the coupled inductor, which does not contribute to the useful energy transfer from the primary to the secondary winding. This energy is generally dissipated as heat, reducing the converter's efficiency and increasing voltage and current stress on the components [13].

Leakage inductance can also cause high-voltage spikes across the power switch, leading to the need for additional protection circuits, such as snubbers, to absorb and dissipate this excess energy [13], [30]. The presence of leakage inductance increases dissipation losses and may lead to stricter insulation requirements and the use of components with higher voltage ratings, which increases PCB layout complexity and raises the overall system cost [31]. The voltage spikes caused by leakage inductance may also reduce the reliability of the converter, as components exposed to high voltage stress are more prone to premature failure [13], [30], [31]. Fig. 1 illustrates the change in the drain-to-source voltage waveform of the switch due to the effects of leakage inductance (c).

Leakage inductance not only affects converter efficiency but can also generate electromagnetic interference (EMI). The EMI generated by voltage spikes may interfere with other electronic devices, leading to electromagnetic compatibility (EMC) issues. To mitigate these effects, it is crucial to implement design techniques that minimize leakage inductance and its associated impacts [13], [30], [31].

In the literature, some methods based on the geometry of coupled inductors are presented for estimating the leakage inductance. According to [30], [32], the leakage inductance formulations employed in their studies are derived from the classical eddy currents in transformer windings formulation introduced by [33]. Building upon this foundation, the leak-

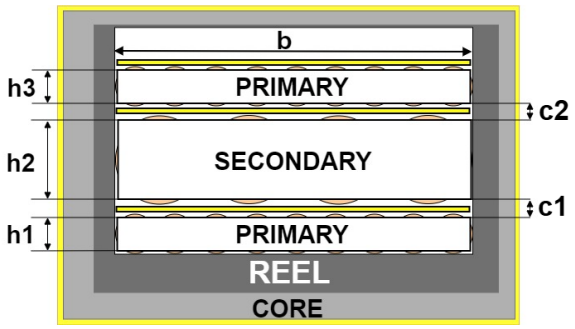

FIGURE 2. Measures used in (1).

age inductance for coupled inductors can be estimated using (1), where μ_o is the magnetic permeability of vacuum, N_P is the number of turns of the primary winding, MLT is the mean length per turn of the coupled inductor as found in the bobbin's datasheet, $\sum h$ is the sum of the heights of all copper winding layers, $\sum c$ is the sum of the heights of the gaps between winding layers, m is the interleaving level, and b is the width of the coil. Fig. 2 illustrates the acquisition of the required measurements to estimate the leakage inductance in a coupled inductor.

$$Llk = \frac{\mu_o \cdot N_P^2 \cdot MLT \cdot (\sum h + 3\sum c)}{3b} \cdot \frac{1}{m^2} \tag{1}$$

The parameter m can be defined as the number of times the magnetomotive force (MMF) within the coupled inductor reaches its peak and returns to zero. A peak in MMF occurs at the spacing between the primary and secondary windings. Therefore, the parameter m depends on the number of interleaved layers between the two windings [30]. The windings, made up of round wires with diameter d, must be converted to an equivalent copper block with height h, as shown in Eq. (2) [33].

$$h = d \cdot \sqrt{\frac{\pi}{4}} \tag{2}$$

The spacing c between the layers is the difference between the diameter d and height h, added to the thickness of the insulation layer i of the copper wire and the thickness t of the tape used for interwinding insulation, as described by (3) [33].

$$c = (d - h) + i + t \tag{3}$$

As observed in Eq. (1), (2), and (3), the estimation of leakage inductance is only based on geometric and construction parameters of the coupled inductor, making its analysis relatively simple.

Leakage inductance is an inherent and ubiquitous phenomenon in coupled inductors. It significantly affects the operation of flyback converters, making the design more complex by requiring additional protection circuits, higher-rated components, and extra care in the printed circuit board (PCB) layout. Therefore, for the implementation of more efficient and reliable flyback converters, the leakage inductance in their coupled inductors must be minimized through proper magnetic element design.

B. SKIN EFFECT

The skin effect is a phenomenon caused by the induction of parasitic currents within the conductor. It is associated with current harmonics at high frequencies flowing through the conductor [30], [34].

In a conductor carrying a direct current or low-frequency current, the internal and surrounding magnetic field is radially symmetric, and the current density within the conductor is homogeneous. Under these conditions, the induction-related losses caused by the magnetic field are negligible when compared to the losses due to the conductor's own resistance [33].

However, at high frequencies, as the current undergoes rapid variations, the magnetic flux within the conductor also changes rapidly. This induces voltage loops inside the conductor. These voltage loops, in turn, induce parasitic currents in the conductor that are in phase with the voltage. These currents add to the main current on the outer layers of the conductor, while opposing it in the inner regions [32].

Due to this behavior of parasitic currents, the current density on the surface of the conductor increases and tends toward zero closer to the center. In other words, the portion of copper that effectively carries current decreases, which causes the conductor's resistance, and consequently the power losses, to become significantly more pronounced at high frequencies [32], [33].

Although the skin effect contributes to the AC conduction losses of coupled inductors, the techniques presented in this paper do not influence it, as this phenomenon depends primarily on the frequency of the current and the diameter of the conductor. On the other hand, the proximity effect, discussed in the following subsection, affects poorly designed coupled inductors in such a way that, in some cases, the losses caused by the skin effect can be neglected [32].

C. PROXIMITY EFFECT

Just as the magnetic field of a conductor affects and induces currents within itself, this magnetic field also affects nearby conductors. The magnetic fields of adjacent conductors add vectorially, causing a non-uniform distribution of the fields on the surfaces of the conductors. As a result, the currents induced by these fields will also be non-uniform [34]. The proximity effect in coupled inductors and transformers causes losses that can be, in magnitude, much greater than conduction losses and those caused by the skin effect [32].

The explanation of the proximity effect is very similar to that of the skin effect. In both cases, parasitic currents are induced in a conductor as a result of the magnetic field of a current-carrying conductor. These parasitic currents generate losses equivalent to an increase in conductor resistance, also known as AC resistance [35].

Unlike the skin effect, the parasitic currents induced by the proximity effect are caused by the magnetic field of an adjacent conductor, as this field penetrates the analyzed conductor perpendicularly [34]. The main current in the conductor adds vectorially to the parasitic currents, causing current concentration on one side of the conductor, since currents in the same direction will have their magnitudes added and those in opposite directions will have their magnitudes subtracted [33].

The proximity effect is amplified when multiple layers are considered as a result of the magnetic field distribution caused by each layer. Due to the presence of the magnetic core, the field on the outermost layer of the inductor is very low. However, the field present in the innermost layers of the inductor is significantly increased [34].

The dissipated power is proportional to the square of the current, making the AC loss of the inductor much higher than the DC loss. The proximity effect is so significant in coupled inductors and transformers that the skin effect can often be disregarded [34].

One way to reduce the proximity effect is to interleave the primary and secondary winding layers of the inductor. In this way, MMF inside the inductor can change polarity, and its peak is reduced [33].

A method to quantify the proximity effect was presented in [33], and is demonstrated through Eq. (4), (5), (6), and (7), where the real part of the result is K, called the proximity factor, a multiplication factor for the winding resistance R_{DC} to obtain an equivalent AC resistance, R_{AC}. In these equations, Re is a function that returns the real part of a complex number, α is the inverse penetration depth, i is the imaginary unit, ω is the angular frequency, f is the frequency, σ is the electrical conductivity of the conductor, η is the porosity factor, N is the number of layers and a is the diameter of the conductor.

$$\omega = 2 \cdot \pi \cdot f \tag{4}$$

$$\eta = N \cdot \frac{a}{b} \tag{5}$$

$$\alpha = \sqrt{i \cdot \omega \cdot \mu_0 \cdot \eta} \tag{6}$$

$$\begin{aligned} K = \frac{R_{AC}}{R_{DC}} &= \mathrm{Re}[\alpha \cdot h \cdot \coth(\alpha \cdot h)] \\ &+ \frac{m^2 - 1}{3} \cdot \left[2 \cdot \alpha \cdot h \cdot \tanh\left(\frac{\alpha \cdot h}{2} \right) \right] \end{aligned} \tag{7}$$

From these calculations, it is possible to determine the losses due to the proximity effect, and consequently, the total copper losses in the coupled inductor. This can be done using Eq. (8) - (12), where $I_{AC_{RMS}}$ is the AC component of the winding's RMS current, I_{RMS} is the total RMS current of the winding, I_{DC} is the average current of the winding, R_{DC} is the resistance of the winding, P_{AC} is the winding loss due to the proximity effect, P_{DC} is the DC loss of the winding, and P_{total} is the total loss of the winding [33]. These calculations were presented in [33] for sinusoidal waveforms. Although most converters do not exhibit this type of waveform, much of the literature analyzing the proximity effect uses this approach to estimate losses [34].

$$I_{AC_{RMS}} = \sqrt{I_{RMS}^2 - I_{DC}^2} \tag{8}$$

$$R_{AC} = K \cdot R_{DC} \tag{9}$$

$$P_{AC} = R_{AC} \cdot I_{AC_{RMS}}^2 \tag{10}$$

$$P_{DC} = R_{DC} \cdot I_{DC}^2 \tag{11}$$

$$P_{total} = P_{AC} + P_{DC} \tag{12}$$

Therefore, it becomes evident that the proximity effect can have a significant impact on coupled inductors, representing a substantial portion of the converter circuit losses. For this reason, the design of coupled inductors aimed at reducing proximity effect losses is crucial to achieving a high-efficiency, high-power-density flyback converter.

IV. LEAKAGE INDUCTANCE REDUCTION

Most of the techniques used to mitigate the effects of leakage inductance in flyback converters, including energy recovery methods and advanced control strategies, require the use of a greater number of components, which increases system cost and may lead to lower power density [6], [10], [11]. Therefore, it is desirable to evaluate ways to reduce the effects of leakage inductance without adding components.

Leakage inductance can be minimized by optimizing the geometry of the windings in a coupled inductor or transformer [20]. Moreover, considering the effects of parasitic currents, as described in [33], is crucial. These currents can increase the resistance of the windings and the leakage inductance, especially at high frequencies.

According to Eq. (1), leakage inductance can be reduced by decreasing the number of turns in the primary winding, the mean length per turn, and the height of the winding layers. On the other hand, increasing the coil width and the interleaving level of the inductor can also reduce leakage inductance.

The application of this method requires that all the winding layers fully occupy the width b of the coil. Partial winding layers will result in higher leakage inductance [30].

When analyzing the available options for reducing leakage inductance, it becomes clear that if a specific magnetic core is preselected, or if there is limited space for the implementation of the coupled inductor, increasing the coil width b becomes unfeasible. The mean length per turn MLT also depends on the bobbin and the core. The number of turns in the primary winding will depend on the required inductance as well as the chosen core and bobbin. Thus, the remaining adjustable parameters are h, c, and m, since μ_0 is a constant.

According to Eq. (2), h depends on the diameter of the copper wires of the inductor, which must be calculated according to the currents and current densities of the primary and secondary windings. Meanwhile, c, according to Eq. 3, also depends on the wire diameters, as well as the thickness of the tape between windings and the insulation layer of the copper wires.

The variable m, in turn, depends on the number of alternating layers between the primary and secondary windings, as a peak in magnetomotive force occurs at the spacing between the two windings [30]. Observing Eq. (1) again, it can be concluded that increasing the interleaving level results in the greatest reduction of leakage inductance, since the parameter m appears squared in the denominator, even though this also inherently increases c due to the additional insulation layers between the winding layers. When m is increased, the effective height of the copper layers h may remain approximately constant if the wire gauge and the number of layers are unchanged, but it can increase when additional layers are introduced to achieve higher interleaving levels, affecting the total winding height and window utilization. Furthermore, higher interleaving levels can also increase manufacturing complexity, winding time, and sensitivity to construction tolerances, which may impact reproducibility in low-cost, mass-produced magnetic components.

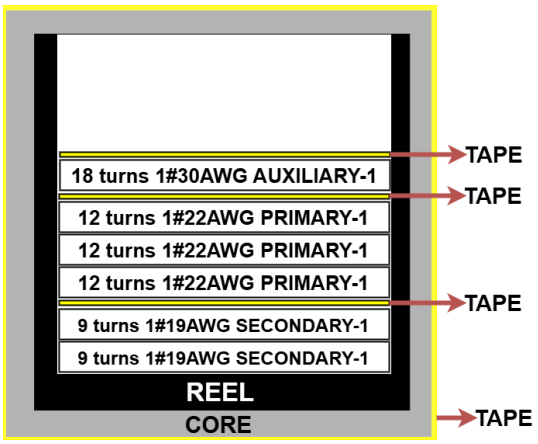

FIGURE 3. Layer diagram of inductor 1.

V. IMPLEMENTATION OF INDUCTORS USING THE INTERLEAVING TECHNIQUE

As explained in Section IV, when there is limited space and a predefined core and bobbin, the implementation of the interleaving technique is the best method for reducing the leakage inductance of a coupled inductor to be used in a quasi-resonant flyback LED driver. To validate this assumption, eleven inductor models with a primary inductance of 250 μH were designed using a PQ3220 magnetic core. Their main characteristics are shown in Table 1, where N_P is the number of turns in the primary winding, AWG_P is the AWG gauge of the primary copper wire, N_S is the number of turns in the secondary winding, N_{aux} is the number of turns in the auxiliary winding, AWG_S is the gauge of the secondary winding copper wire, AWG_{Aux} is the gauge of the auxiliary winding (used to supply power to the control circuitry), m is the interleaving level of the inductor, and t is the number of tape layers, each with a thickness of 0.1 mm. Fig. 3 shows the layer diagram of inductor 1. The other inductors were designed following the same layout standard, according to the layer division and number of windings of each one.

It is important to highlight that some design parameters, such as the number of turns and wire gauges, were intentionally modified among prototypes to explore the combined influence of winding geometry and interleaving on leakage inductance and proximity losses. Although interleaving was the main design variable, these adjustments reflect practical trade-offs typically encountered in LED driver magnetic design, enabling a broader evaluation of performance under realistic conditions.

Although all inductors in Table 1 were modeled using the same mean length per turn (MLT = 66 mm) obtained from the PQ3220 bobbin datasheet, the effective MLT may vary slightly with the number of winding layers. Inductors with fewer layers tend to have a smaller average turn length, while those with more layers exhibit a slightly higher MLT due to the radial build of the winding. In practical implementations, additional variations also occur because of minor winding imperfections, such as uneven wire tension, non-uniform

TABLE 1. Constructive characteristics of the implemented coupled inductors

Inductor	N_P	AWG_P	$N_S = N_{aux}$	AWG_S	AWG_{aux}	m	t [mm]	MLT	b [mm]	$\sum h$ [mm]	$\sum c$ [mm]
1	36	22	18	19	30	2	2	66	9.1	4.1	0.6
2	32	26	16	26	30	2	3	66	9.1	3.1	0.5
3	32	26	16	26	30	2	3	66	9.1	3.1	0.5
4	32	26	16	26	30	4	4	66	9.1	3.1	0.6
5	32	26	16	26	30	4	5	66	9.1	3.1	0.6
6	32	26	16	26	30	4	6	66	9.1	3.1	0.7
7	32	26	16	26	30	4	6	66	9.1	3.1	0.7
8	32	26	16	26	30	4	9	66	9.1	3.1	0.8
9	32	26	18	26	30	5	9	66	9.1	3.2	0.9
10	28	26	14	26	30	4	7	66	9.1	3.1	0.8
11	32	26	16	26	30	5	8	66	9.1	3.2	0.9

stacking, and small misalignment between layers. However, these effects result in minor deviations, and therefore have a very small impact on the evaluation of leakage inductance.

The estimation of the leakage inductance of each inductor was calculated according to Eq. (1). Table 2 presents a comparison between the calculated leakage inductance and the measured leakage inductance of the implemented inductors, where L_{lk} is the measured leakage inductance, including an absolute deviation due to the measurement range error of the equipment used, $L_{lk}\%$ is the percentage of leakage inductance in relation to the primary inductance, $L_{lk}C$ is the calculated leakage inductance, and $Error\%$ is the percentage error between the calculated and measured leakage inductance.

According to the data in Table 2, the largest deviation between the calculated and measured leakage inductances slightly exceeds 30%. However, in absolute terms, this difference corresponds to only 1.311 µH, which represents merely 0.5244% of the total primary inductance (250 µH). This normalization to the total primary inductance is intended to emphasize that, although the relative error appears high, it results from the very small magnitude of the leakage inductance itself when compared to the magnetizing inductance. Moreover, the measurement equipment presents an uncertainty of 3.23% within the range in which the largest error was detected. Additionally, absolute deviations below 15 nH were obtained for several samples, confirming that Eq. (1) provides a reliable approximation of the leakage inductance in coupled inductors. The main contributors to the observed error are small deviations in the physical implementation of parameters t and h, as well as manual winding tolerances.

TABLE 2. Comparison between measured and calculated leakage inductance in the implemented coupled inductors.

Ind.	L_{lk}	$L_{lk}\%$	$L_{lk}C$	Error %
1	$4.730\ \mu\text{H} \pm 0.138\ \mu\text{H}$	1.892%	$5.364\ \mu\text{H}$	11.82%
2	$3.320\ \mu\text{H} \pm 0.103\ \mu\text{H}$	1.328%	$4.047\ \mu\text{H}$	17.96%
3	$2.736\ \mu\text{H} \pm 0.088\ \mu\text{H}$	1.094%	$4.047\ \mu\text{H}$	32.39%
4	$1.333\ \mu\text{H} \pm 0.053\ \mu\text{H}$	0.533%	$1.070\ \mu\text{H}$	−24.58%
5	$1.289\ \mu\text{H} \pm 0.052\ \mu\text{H}$	0.515%	$1.128\ \mu\text{H}$	−14.27%
6	$1.168\ \mu\text{H} \pm 0.049\ \mu\text{H}$	0.467%	$1.187\ \mu\text{H}$	1.63%
7	$0.873\ \mu\text{H} \pm 0.041\ \mu\text{H}$	0.349%	$0.939\ \mu\text{H}$	7.03%
8	$0.835\ \mu\text{H} \pm 0.040\ \mu\text{H}$	0.334%	$0.784\ \mu\text{H}$	−6.51%
9	$0.770\ \mu\text{H} \pm 0.039\ \mu\text{H}$	0.308%	$0.784\ \mu\text{H}$	1.79%
10	$0.737\ \mu\text{H} \pm 0.038\ \mu\text{H}$	0.294%	$0.741\ \mu\text{H}$	0.54%
11	$0.694\ \mu\text{H} \pm 0.037\ \mu\text{H}$	0.277%	$0.702\ \mu\text{H}$	1.14%

VI. RESULTS

Based on the designed inductors, a high power factor 60 W quasi-resonant flyback LED driver with an output voltage of approximately 50 V was designed with the objective of measuring the drain-to-source voltage spikes of the main switch, the system efficiency, and the temperature of critical components. An 800 V breakdown voltage MOSFET was used as the switch. To prevent the drain-to-source voltage spikes from causing catastrophic failure in the driver, an RCD snubber circuit was designed to ensure that the voltage would not exceed approximately 90% of the break-

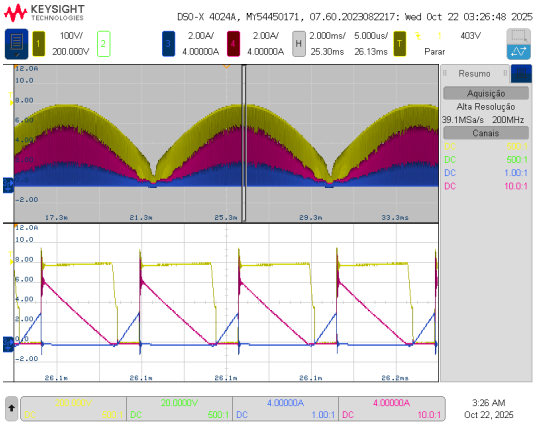

FIGURE 4. QR operation of the converter: drain-to-source voltage waveform (yellow), primary magnetizing current (blue), and secondary magnetizing current (pink).

down voltage of the switch under the worst-case leakage inductance condition. The same snubber circuit was used for all evaluated cases. The snubber circuit was designed according to Eq. (13), derived from [36], where V_{clamp} is the clamping voltage of the snubber circuit, V_{ORmax} is the maximum output voltage reflected to the primary, R_{clamp} is the resistance of the snubber circuit, L_{lk} is the leakage inductance, P_i is the input power of the converter, and L_p is the primary inductance of the coupled inductor.

$$V_{clamp} = V_{ORmax} + \frac{\sqrt{V_{ORmax}^2 + 4 \cdot R_{clamp} \cdot L_{lk} \cdot \frac{P_i}{L_p}}}{2} \tag{13}$$

The designed RCD snubber circuit yielded a theoretical value of $R_{clamp} = 94.036\ k\Omega$. In practice, a resistance of $94\ k\Omega$ was used through association.

The quasi-resonant flyback converter with integrated power factor correction exhibits a typical switching frequency modulation along the rectified mains waveform. The minimum frequency occurs near the mains peaks, while the maximum frequency appears close to the valleys. For input voltages of 100 V, 127 V, 220 V, and 277 V, the switching frequency varies approximately within the ranges of 56–62 kHz, 66–77 kHz, 86–116 kHz, and 90–142 kHz, respectively. The controller used in the prototype does not perform valley-skipping. Therefore, the switch is always activated at the first valley of the drain-to-source voltage oscillation.

Fig. 4 represents the quasi-resonant operation of the implemented converter, showing the drain-to-source voltage, primary magnetizing current, and secondary magnetizing current, while Fig. 5 illustrates the drain-to-source voltage peak measured at low frequency, using inductor 11, which has the lowest leakage inductance, with the converter operating at an input voltage of 220 V, and its peak of 533 V.

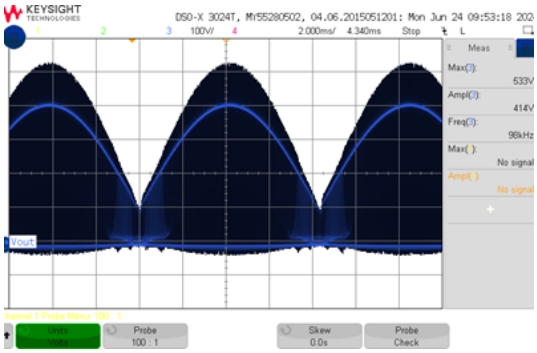

FIGURE 5. Drain-to-source voltage at low frequency and 533 V peak.

Dynamic behavior tests were performed to evaluate the transient response of the proposed converter under load and input voltage variations. Figure 6 presents the converter operation at 220 V input during an input power step from 60 W to 30 W, demonstrating its capability for dimming applications. The input and output voltage and current waveforms show that the converter maintains a sinusoidal input current with power factor correction and a regulated output.

Figure 7 shows the converter response to a line-voltage step, where the input voltage was varied from 127 V to 220 V and then back to 127 V. The results confirm that the converter continues to operate properly under wide line variations, with stable output regulation and no distortion or transient spikes in the input current waveform.

It is important to note that the qualitative shape of the input and output voltage and current waveforms does not change significantly among the eleven implemented inductors, since the control method, operating conditions, and regulation mechanisms remain identical. Therefore, these waveforms are presented only to demonstrate the correct operation of the converter, while the influence of each magnetic design is evaluated through the quantitative performance metrics discussed further in this section.

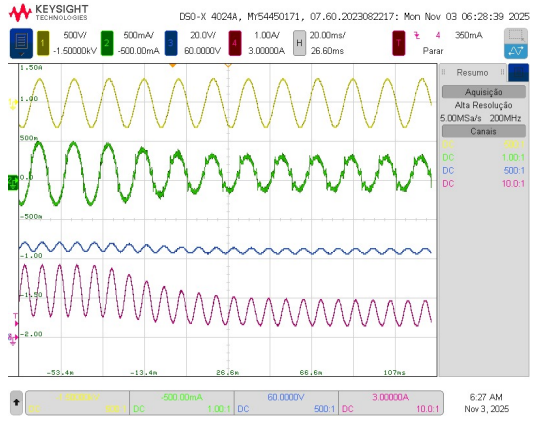

FIGURE 6. Experimental waveforms of the quasi-resonant flyback converter during an input power step from 60 W to 30 W at 220 V input: input voltage (yellow), input current (green), output voltage (blue), and output current (pink).

A. EFFICIENCY, VOLTAGE PEAK, AND THERMAL ANALYSIS

Using the designed converter, the voltage peak across the switch, the efficiency of the converter, and the temperatures measured on the switch, the snubber circuit, and the coupled inductor were measured at the input voltages of 100, 127, 220, and 277 V. Table 3 shows these measurements using each of the eleven designed coupled inductors, where $V_{ds_{pk}}$ is the measured drain-to-source voltage peak, T_s is the temperature measured on the main power switch, T_{sn} is the temperature measured on the snubber circuit, and T_L is the temperature measured on the copper of the coupled inductor.

It is worth noting that all measurements of efficiency, switch voltage peak, and thermal performance were conducted under full-load conditions, as this represents the worst-case scenario for evaluating the effects of leakage inductance and associated losses. Testing at this operating point ensures that the influence of magnetic design parameters is clearly observable, while the dynamic tests validate the stability and robustness of the proposed converter under varying load and line conditions.

Fig. 8 and 9 illustrate the measured efficiency and MOSFET drain-to-source voltage peak ($V_{DS_{peak}}$) obtained for each implemented inductor at a 220 V input. In both graphs, the x-axis represents the inductor number, with the corresponding interleaving level m indicated in parentheses. The y-axis represents efficiency in the first graph and the measured $V_{DS_{peak}}$ in the second. These results show that inductors with higher coupling, generally achieved through greater interleaving levels, tend to exhibit higher efficiency and lower voltage peaks. However, this trend is not exclusively defined by the interleaving level, since other geometric and construction parameters, such as the number of turns, turns ratio, conductor wire gauge, layer spacing c, winding height h, and window utilization, also influence copper losses, coupling, and leakage energy. Therefore, these graphs provide a global comparison of the magnetic performance of each prototype at a 220 V input, highlighting the combined effect of interleaving and geometric factors on converter efficiency and voltage stress.

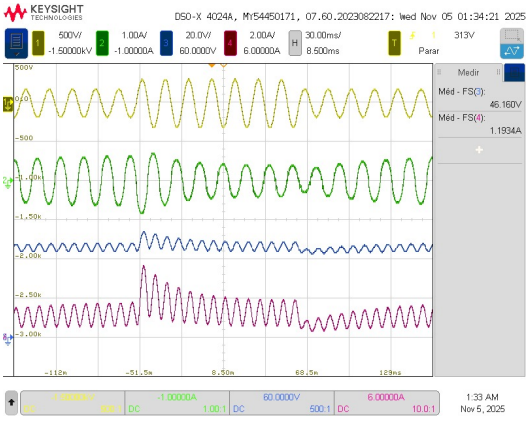

FIGURE 7. Experimental waveforms of the quasi-resonant flyback converter during a line-voltage step from 127 V to 220 V and back to 127 V: input voltage (yellow), input current (green), output voltage (blue), and output current (pink).

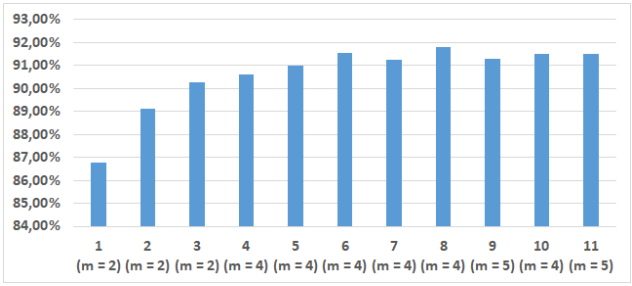

FIGURE 8. Converter overall efficiency at 220 V input for each coupled inductor and its interleaving level.

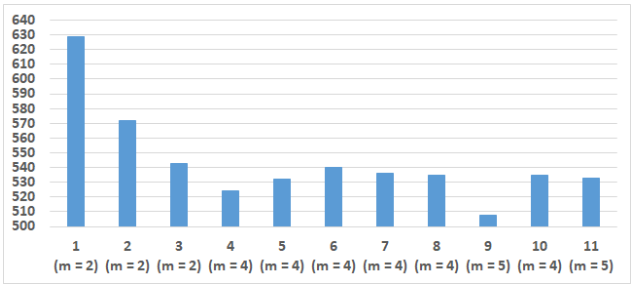

FIGURE 9. Drain-to-source voltage peak at 220 V input for each coupled inductor and its interleaving level.

Table 4 presents the measured clamp voltage V_{clamp} using each implemented inductor at 220 V input voltage, and the corresponding snubber power dissipation P_{snRCD} calculated through Eq. (14). For a normalized efficiency comparison, the input power P_{in}, the output power P_{out} and a normalized efficiency disregarding the snubber losses η_{norm} are also shown in Table 4, with the former being calculated by Eq. 15).

$$P_{snRCD} = \frac{V_{clamp}^2}{R_{clamp}} \tag{14}$$

$$\eta_{\text{norm}} = \frac{P_{in}}{P_{out} - P_{snRCD}} \tag{15}$$

The normalized efficiency values presented in Table 4 show an improving trend among the prototypes, indicating that the magnetic design significantly affects converter performance. Inductors with an enhanced design exhibit higher normalized efficiencies. Although the normalization process excludes the snubber losses from the efficiency calculation, it is important to note that inductors with lower leakage inductance also lead to smaller voltage spikes. This reduction in overvoltage inherently decreases the energy dissipated in the RCD snubber, contributing to the overall improvement in efficiency. Additionally, Inductor 9 presented the lowest clamp voltage, mainly due to its lower turns ratio, which

TABLE 3. Efficiency, drain-to-source voltage peaks, and measured temperatures.

	100 V					127 V					220 V					277 V				
Ind.	η [%]	$V_{ds_{pk}}$ [V]	T_s [°C]	T_{sn} [°C]	T_L [°C]	η [%]	$V_{ds_{pk}}$ [V]	T_s [°C]	T_{sn} [°C]	T_L [°C]	η [%]	$V_{ds_{pk}}$ [V]	T_s [°C]	T_{sn} [°C]	T_L [°C]	η [%]	$V_{ds_{pk}}$ [V]	T_s [°C]	T_{sn} [°C]	T_L [°C]
1	83.15	462	113	113	101	84.84	508	101	114	105	86.77	629	98	112	105	86.49	713	102	115	105
2	87.13	431	101	96	97	88.42	451	89.5	91	93	89.13	572	88	93	95	88.40	666	99	101	99
3	88.56	398	96	85	88	89.76	412	86	84	85	90.29	543	83	88	86	89.64	641	91	96	90.5
4	89.16	353	93.5	82.5	80	90.18	386	85.5	78.5	78.9	90.60	524	80	82	78.5	90.00	617	90	89	90
5	89.31	349	94.5	74	78.4	90.44	391	84.5	74	77	91.00	532	80	82	77.8	90.45	645	80	81	79
6	89.59	375	91.8	77	74	90.47	407	82	76	71	91.56	540	79.5	76.5	76	91.45	622	80.6	69.4	69.4
7	89.32	371	94.2	73	73	90.52	371	86	66	70.9	91.25	536	76	75	70.5	90.59	607	81	68	70
8	89.55	362	90	68	69	91.03	397	81	75	68	91.80	535	76.7	67	67	91.53	600	78	66	66
9	89.63	327	90	77	68	90.72	368	81	72	67	91.29	508	75	66	66	91.57	586	77	67	67
10	89.36	330	90	75	70	90.66	390	80	66	66	91.49	535	76	61.4	64.5	91.00	618	75.8	62.8	66
11	89.45	359	90	74	70	90.70	393	79.5	60	66	91.50	533	76	63	67	91.00	616	78	63	67

TABLE 4. Measured clamp voltage, snubber losses, input power, output power, and normalized efficiency for each coupled inductor at 220 V input voltage.

Inductor	$V_{\textbf{clamp}}$ [V]	$P_{\textbf{snRCD}}$ [W]	P_{in} [W]	P_{out} [W]	η_{norm} [%]
1	183.0	0.356	61.75	53.58	87.27
2	168.0	0.300	60.62	54.03	89.57
3	169.8	0.307	59.82	54.02	90.77
4	157.2	0.263	59.54	53.95	91.01
5	159.0	0.269	59.63	54.27	91.42
6	138.5	0.204	59.23	54.29	92.45
7	157.0	0.262	59.31	54.13	91.67
8	150.0	0.239	59.47	54.60	92.18
9	127.2	0.172	59.51	54,32	91.54
10	147.4	0.234	59.32	54.28	91.87
11	151.8	0.245	59.33	54.29	91.88

reduces the reflected voltage on the primary side and consequently the snubber voltage stress.

Based on the presented results, an improvement in the efficiency of the converter can be observed with the reduction of leakage inductance, as well as a decrease in the temperature of the components. These aspects are likely caused by the reduction in inductor copper losses, due to the decrease in AC resistance caused by parasitic currents from the proximity effect, and the reduction of the drain-to-source voltage peak, which lowers the switching losses and the power dissipated by the snubber circuit.

B. PROXIMITY EFFECT LOSSES ESTIMATION

To evaluate the proximity effect losses in each implemented coupled inductor, an approach based on section III-C was used. The analysis was conducted using data acquired at 220 V input. First, the power required for the coupled inductor to reach the measured temperatures was simulated through FEM, then divided between primary conduction losses and secondary conduction losses. The resistance R_{DC} of each winding of each coupled inductor was measured, as were the mean and RMS currents, I_{DC} and I_{RMS}. Using these measurements, the DC losses on the coupled inductors were calculated through Eq. (11). Using Eq. (12), the DC losses were deducted from the simulated total losses P_{total}, resulting in the estimated AC losses P_{AC}. Through Eq. (8), the AC RMS current was calculated for each winding, and by Eq. (10), the AC equivalent resistances were obtained. Finally, the proximity factor K was calculated through Eq. (9).

Table 5 shows the results of those estimations on the primary, where $P_{total_{pri}}$ are the primary total losses, P_{CCpri} are the primary DC losses, P_{ACpri} represents the primary AC losses, R_{ACpri} represents the primary AC equivalent resistances, and K_{pri} represents the primary proximity factors.

Table 6 shows the results of the estimations on the secondary, where $P_{total_{sec}}$ are the secondary total losses, P_{CCsec} are the primary DC losses, P_{ACsec} represent the secondary AC losses, R_{ACsec} represent the secondary AC equivalent resistances, and K_{sec} represent the primary proximity factors.

TABLE 5. Estimation of conduction and proximity effect losses in the primary winding of implemented coupled inductors at 220 V input voltage.

Inductor	$P_{total_{pri}}$ [mW]	P_{CCpri} [mW]	P_{ACpri} [mW]	R_{ACpri} [mΩ]	K_{pri}
1	461	11.3	449.5	1102	8.1
2	457	10.9	445.8	1167	8.58
3	293	11.4	281.7	711	5.08
4	242	11.7	229.9	605	3.95
5	253	11.8	240.7	625	4.17
6	244	11.7	231.9	609	3.8
7	219	11.4	207.9	544	3.51
8	217	9.9	207.4	555	3.86
9	256	9.6	246.3	746	4.6
10	203	8.5	194.1	513	3.66
11	276	11.4	264.7	711	4.44

TABLE 6. Estimation of conduction and proximity effect losses in the secondary winding of implemented coupled inductors at 220 V input voltage

Inductor	$P_{total_{sec}}$ [mW]	P_{CCsec} [mW]	P_{ACsec} [mW]	R_{ACsec} [mΩ]	K_{sec}
1	1872	45.6	1826	442	12.992
2	1744	43.7	1700	414	12.555
3	1392	51.4	1341	317	8.574
4	1108	50.4	1057	254	6.872
5	1200	55.5	1144	271	6.764
6	1074	53.1	1021	245	6.441
7	1034	57.5	977	238	5.667
8	978	46.8	931	233	6.484
9	1094	41.1	1053	351	9.240
10	909	44.6	865	281	6.226
11	1148	45.9	1002	249	7.119

Observing Tables 5 and 6, it is evident that the reduction in the temperature of the coupled inductors obtained with the application of the interleaving technique is primarily associated with the mitigation of proximity effect losses. This is particularly clear when comparing inductors 1 to 3, non-interleaved or poorly interleaved, which exhibit high proximity factors and significantly larger AC losses, with inductors 4 to 11, where better interleaving and geometric optimization result in lower K values, as low as 3.5.

In the primary winding, total losses obtained by the estimation decreased from 461 mW in Inductor 1 to values as low as 203 mW in Inductor 10, even though DC conduction losses remained nearly constant across all samples. This reinforces the role of geometry and interleaving. Similarly, in the secondary winding, inductors 1 and 2 reached over 1.7 W of estimated AC losses, while inductors 6 to 11 remained close to or below 1 W, with significantly lower R_{AC} and K_{sec} values.

In conclusion, the proper interleaving and magnetic design not only reduce voltage stress and switching losses but also improve thermal behavior and efficiency. This confirms that careful inductor design can have a systemic positive impact on quasi-resonant flyback converters, supporting the use of advanced interleaving strategies in high-performance LED drivers.

C. ELECTROMAGNETIC INTERFERENCE (EMI) ANALYSIS

Since leakage inductance also influences drain-to-source voltage spikes and high-frequency switching behavior, conducted EMI measurements were performed to further evaluate the impact of winding geometry on converter performance. Conducted emission tests were performed according to [37] using the LISN method, within the frequency range from 9 kHz to 30 MHz. The measurement setup followed the same standard, employing a real-time spectrum analyzer RSA3030E-TG and a KH3760 LISN.

The first test was conducted using Inductor 2, which has a poor design and high leakage inductance. In contrast, the second one was conducted using Inductor 8, which has the same turns ratio and number of primary turns, and is not the most complex inductor implemented. However, it achieved a 74.84% reduction in leakage inductance if compared to Inductor 2.

Fig. 10 demonstrates the results obtained using inductor 2, while Fig. 11 shows the results obtained using inductor 8. In both, the orange straight lines represent the limits for quasi-peak measures, while the blue straight lines represent the limits for average measures. The emissions represented in orange color are the peak emission levels, while the emissions represented in blue color are the average emission levels.

Analyzing both figures, there is a clear reduction in both peak and average emission levels when using a coupled inductor with lower leakage inductance. This reduction can

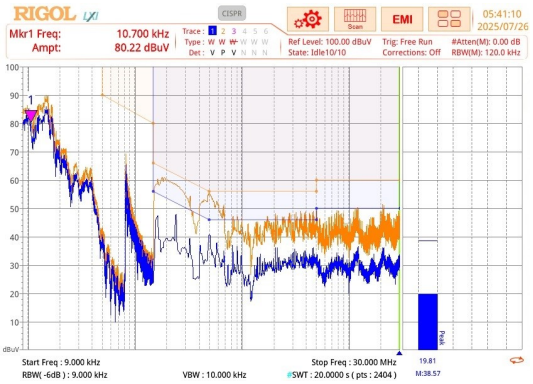

FIGURE 10. Conducted emissions obtained accordingly to CISPR 15:2013 using Inductor 2 in the implemented LED driver.

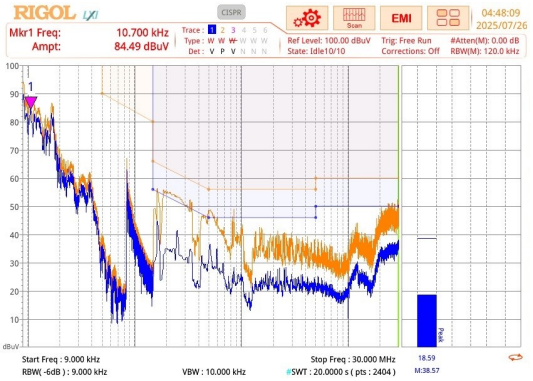

FIGURE 11. Conducted emissions obtained accordingly to CISPR 15:2013 using Inductor 8 in the implemented LED driver.

be observed mainly in the range from 100 kHz to 10 MHz, where the emissions obtained using the coupled inductor with lower leakage inductance are nearly 10 dB lower than the measured emissions using a poorly designed coupled inductor.

According to the facts discussed before, lower leakage inductances retain less energy, which causes a reduction in high-frequency resonance in the converter. These results show that, besides reducing the proximity effect, the interleaving technique can also help EMI compliance by reducing leakage inductance.

VII. CONCLUSION

This work presented a comprehensive investigation of the design of coupled inductors for quasi-resonant flyback LED drivers, focusing on mitigating leakage inductance effects without increasing the number of components. Through the application of the interleaving technique and the geometric optimization of windings, a total of eleven inductors were implemented and evaluated.

The analytical approximation of leakage inductance proved to be consistent with measured values, demonstrating its applicability to practical design. Experimental results showed that increasing the interleaving level leads to a significant reduction in leakage inductance, which, in turn, contributes to lower voltage spikes across the main power switch, reduced thermal stress, and improved overall efficiency.

Additionally, the impact of the proximity effect on winding losses was analyzed through experimental estimation based on copper temperatures and FEM simulations. The results highlighted that coupled inductors designed using the interleaving technique not only improve system performance but also mitigate proximity losses, resulting in enhanced power density and thermal performance.

Furthermore, the electromagnetic interference (EMI) analysis confirmed that lower leakage inductance directly contributes to the reduction of conducted emissions. Measurements following the CISPR 15:2013 standard showed significantly lower peak and average EMI levels when optimized inductors were used. This reinforces that proper magnetic design not only improves efficiency and thermal behavior but also aids in regulatory compliance.

Therefore, the adoption of advanced magnetic design techniques, such as interleaving, is shown to be an effective and low-cost strategy for optimizing quasi-resonant flyback converters for LED lighting applications, achieving high efficiency, power density, and EMI performance without compromising reliability.

In spite of the fact that the study focused on PQ-type cores, the methodology can be extended to other core families with rectangular windows, such as E and pot cores. The same analytical approach applies, requiring only the adaptation of geometric parameters to the specific core shape.

For toroidal structures, Eq.1 is not directly applicable without additional modeling. A direct comparison with other structures, such as planar inductors or integrated magnetics, was also not performed, as these present distinct construction methods and design trade-offs. In contrast, the proposed method focuses on conventional converters and inductors, offering a simple and cost-effective solution suitable for mass production.

Although the analysis was conducted for a 60 W input LED driver, the proposed design methodology is scalable to higher power levels. However, it is important to note that the flyback topology inherently presents practical power limitations due to increased peak current, coupled inductor leakage energy, and switching losses as the power rises. For higher-power converters, increased current density may require thicker wires or multiple parallel strands, but the same interleaving principles remain valid to balance coupling and minimize AC losses.

Additional details, extended analysis, and complementary discussions related to the magnetic modeling and experimental methodology presented in this work can be found in [38], which further expands the results reported here.

ACKNOWLEDGMENT

This work was supported in part by Zagonel Iluminação S.A.; Empresa Brasileira de Pesquisa e Inovação Indus-

trial (EMBRAPII); the Coordenação de Aperfeiçoamento de Pessoal de Nível Superior – Brasil (CAPES/PROEX) – Finance Code 001; PRPGP/UFSM; and the Conselho Nacional de Desenvolvimento Científico e Tecnológico (CNPq), Brazil, under Grants 403808/2023-5, 403036/2024-0, and 302764/2025-9.

AUTHOR'S CONTRIBUTIONS

J.R.C.AMADO: Conceptualization, Formal Analysis, Funding Acquisition, Investigation, Methodology, Validation, Writing – Original Draft. **K.S.A.ALI:** Investigation, Writing – Review & Editing. **G.K.GRASSI:** Writing – Review & Editing. **H.A.LOBO:** Writing – Review & Editing. **R.R.DUARTE:** Conceptualization, Data Curation, Formal Analysis, Methodology, Supervision, Writing – Original Draft, Writing – Review & Editing. **M.A.D.COSTA:** Methodology, Project Administration, Resources, Supervision, Visualization, Writing – Review & Editing.

PLAGIARISM POLICY

This article was submitted to the similarity system provided by Crossref and powered by iThenticate – Similarity Check.

DATA AVAILABILITY

The data used in this research is available in the body of the document.

REFERENCES

[1] J. R. C. Amado, K. S. A. Ali, R. R. Duarte, H. Lobo, G. Grassi, M. A. D. Costa, "Técnicas de Redução da Indutância de Dispersão em Indutores Acoplados Utilizados em Conversores Flyback Quase Ressonantes como Drivers de LEDs", *in Proceedings of the 16th Seminar on Power Electronics and Control (SEPOC)*, Santa Maria, Brasil, 2024, doi:10.53316/sepoc2024.019.

[2] G. Z. Abdelmessih, J. M. Alonso, M. S. Perdigão, "Hybrid series-parallel PWM dimming technique for integrated-converter-based HPF LED drivers", *in 2016 51st International Universities Power Engineering Conference (UPEC)*, pp. 1–6, 2016, doi:10.1109/UPEC.2016.8113996.

[3] H. van der Broeck, G. Sauerlander, M. Wendt, "Power driver topologies and control schemes for LEDs", *in APEC 07 - Twenty-Second Annual IEEE Applied Power Electronics Conference and Exposition*, pp. 1319–1325, 2007, doi:10.1109/APEX.2007.357686.

[4] J.-M. Wang, C.-W. Lin, K.-Y. Huang, J.-S. Wong, "The Novel Quasi-Resonant Flyback Converter With Autoregulated Structure for Parallel/Serial Input", *IEEE Transactions on Industrial Electronics*, vol. 67, no. 2, pp. 992–1004, 2020, doi:10.1109/TIE.2019.2902827.

[5] S. Dutta, D. Maiti, A. K. Sil, S. K. Biswas, "A Soft-Switched Flyback converter with recovery of stored energy in leakage inductance", *in 2012 IEEE 5th India International Conference on Power Electronics (IICPE)*, pp. 1–5, 2012, doi:10.1109/IICPE.2012.6450415.

[6] J.-W. Kim, I.-O. Lee, G.-W. Moon, K.-B. Park, "Series input parallel output interleaved flyback converter with regenerative leakage inductance energy", *in Proceedings of The 7th International Power Electronics and Motion Control Conference*, vol. 2, pp. 1347–1352, 2012, doi:10.1109/IPEMC.2012.6258993.

[7] Z. Ouyang, J. Zhang, W. G. Hurley, "Calculation of Leakage Inductance for High-Frequency Transformers", *IEEE Transactions on Power Electronics*, vol. 30, no. 10, pp. 5769–5775, 2015, doi:10.1109/TPEL.2014.2382175.

[8] R. Prieto, J. Cobos, O. Garcia, P. Alou, J. Uceda, "High frequency resistance in flyback type transformers", *in APEC 2000. Fifteenth Annual IEEE Applied Power Electronics Conference and Exposition (Cat. No.00CH37058)*, vol. 2, pp. 714–719 vol.2, 2000, doi:10.1109/APEC.2000.822583.

[9] T. Strous, G. Simonelli, "Improved Power Transformer Performance using Leakage Inductance Shielding", *in 2019 European Space Power Conference (ESPC)*, pp. 1–6, 2019, doi:10.1109/ESPC.2019.8932074.

[10] Y.-K. Lo, J.-Y. Lin, "Active-Clamping ZVS Flyback Converter Employing Two Transformers", *IEEE Transactions on Power Electronics*, vol. 22, no. 6, pp. 2416–2423, 2007, doi:10.1109/TPEL.2007.909285.

[11] C.-S. Liao, K. M. Smedley, "Design of high efficiency Flyback converter with energy regenerative snubber", *in 2008 Twenty-Third Annual IEEE Applied Power Electronics Conference and Exposition*, pp. 796–800, 2008, doi:10.1109/APEC.2008.4522812.

[12] R. K. Kokkonda, R. Beddingfield, S. Bhattacharya, B. Carsten, B. Varga, "A Novel Transformer Leakage Energy Recovery Active Clamp Control Technique for High Power AC/DC Flyback Converters", *in 2023 IEEE Applied Power Electronics Conference and Exposition (APEC)*, pp. 1238–1245, 2023, doi:10.1109/APEC43580.2023.10131320.

[13] G. N. Wooding, A. S. De Beer, "The effect of leakage inductance and snubbing on electromagnetic interference generated by a flyback converter", *in IEEE Africon '11*, pp. 1–5, 2011, doi:10.1109/AFRCON.2011.6072057.

[14] C. Larouci, J.-P. Keradec, J.-P. Ferrieux, L. Gerbaud, J. Roudet, "Copper losses of flyback transformer: search for analytical expressions", *IEEE Transactions on Magnetics*, vol. 39, no. 3, pp. 1745–1748, 2003, doi:10.1109/TMAG.2003.810411.

[15] F. A. Holguin, R. Prieto, R. Asensi, J. A. Cobos, "Power losses calculations in windings of gapped magnetic components: The i2D method applied to flyback transformers", *in 2015 IEEE Energy Conversion Congress and Exposition (ECCE)*, pp. 5675–5681, 2015, doi:10.1109/ECCE.2015.7310457.

[16] N. Y. Veretennikov, Y. V. Skitsky, "Loss Optimization Approach in Flyback Transformer Windings", *in 2024 IEEE 25th International Conference of Young Professionals in Electron Devices and Materials (EDM)*, pp. 1290–1293, 2024, doi:10.1109/EDM61683.2024.10615169.

[17] W. Yuan, X. Huang, P. Meng, G. Zhang, J. Zhang, "An improved winding loss analytical model of Flyback transformer", *in 2010 Twenty-Fifth Annual IEEE Applied Power Electronics Conference and Exposition (APEC)*, pp. 433–438, 2010, doi:10.1109/APEC.2010.5433633.

[18] T. Halder, "Improved coupled inductor loss optimization of the Flyback SMPS", *in 2013 International Conference on Power, Energy and Control (ICPEC)*, pp. 798–802, 2013, doi:10.1109/ICPEC.2013.6527764.

[19] H. Onay, V. Süel, T. Özgen, A. Hava, "Comparative Power Loss Analysis of DCM Flyback Transformer Based on FEA, Numeric Simulation, Calculation and Measurements", *in 2019 21st European Conference on Power Electronics and Applications (EPE '19 ECCE Europe)*, pp. P.1–P.10, 2019, doi:10.23919/EPE.2019.8915387.

[20] C. Sullivan, T. Abdallah, T. Fujiwara, "Optimization of a flyback transformer winding considering two-dimensional field effects, cost and loss", *in APEC 2001. Sixteenth Annual IEEE Applied Power Electronics Conference and Exposition (Cat. No.01CH37181)*, vol. 1, pp. 116–122 vol.1, 2001, doi:10.1109/APEC.2001.911636.

[21] Y. Panov, M. Jovanovic, "Adaptive off-time control for variable-frequency, soft-switched flyback converter at light loads", *IEEE Transactions on Power Electronics*, vol. 17, no. 4, pp. 596–603, 2002, doi:10.1109/TPEL.2002.800958.

[22] R. D. Stracquadaini, "Mixed Mode control (Fixed off Time Quasi Resonant) for flyback converter", *in IECON 2010 - 36th Annual Conference on IEEE Industrial Electronics Society*, pp. 556–561, 2010, doi:10.1109/IECON.2010.5675222.

[23] V. Vorperian, "Quasi-square-wave converters: topologies and analysis", *IEEE Transactions on Power Electronics*, vol. 3, no. 2, pp. 183–191, 1988, doi:10.1109/63.4348.

[24] J.-S. Yoo, J.-O. Baek, T.-Y. Ahn, "A High-Efficiency QR Flyback DC–DC Converter with Reduced Switch Voltage Stress Realized by Applying a Self-Driven Active Snubber (SDAS)", *Energies*, vol. 16, no. 3, 2023, doi:10.3390/en16031068.

[25] S. L. Jeng, M. T. Peng, C. Y. Hsu, W. H. Chieng, J. P. Shu, "Quasi-Resonant Flyback DC/DC Converter Using GaN Power Transistors", *World Electric Vehicle Journal*, vol. 5, no. 2, pp. 567–573, 2012, doi:10.3390/wevj5020567.

[26] T. Instruments, "Inductor and Flyback Transformer Design", *Texas Instruments*, pp. 1–19, 2001.

[27] H. Zenkner, "Coupled Inductors and their Applications", *in 2019 International Symposium on Electromagnetic Compatibility - EMC EUROPE*, pp. 963–967, 2019, doi:10.1109/EMCEurope.2019.8871541.
[28] T.-J. Liang, K.-H. Chen, J.-F. Chen, "Primary Side Control For Flyback Converter Operating in DCM and CCM", *IEEE Transactions on Power Electronics*, vol. 33, no. 4, pp. 3604–3612, 2018, doi:10.1109/TPEL.2017.2709811.
[29] D. Carey, "Isolated Switch-Mode Power Supplies: How to Choose a Forward vs. a Flyback Converter", *Analog Devices Techinical Articles*, pp. 1–6, 2024.
[30] B. Keogh, I. Cohen, "Flyback transformer design considerations for efficiency and EMI", *Texas Instruments*, pp. 1–37, 2016.
[31] K. Hashimoto, T. Okuda, T. Hikihara, "A Flyback Converter with SiC Power MOSFET Operating at 10 MHz: Reducing Leakage Inductance for Improvement of Switching Behaviors", *in 2018 International Power Electronics Conference (IPEC-Niigata 2018 -ECCE Asia)*, pp. 3757–3761, 2018, doi:10.23919/IPEC.2018.8507361.
[32] B. Carsten, "High Frequency Conductor Losses in Switchmode Magnetics", pp. 1–91, 1986.
[33] P. L. Dowell, "Effects of eddy currents in transformer windings", *in Proceedings of the IEE*, 1966, doi:10.1049/piee.1966.0236.
[34] L. H. Dixon, "Deriving the Equivalent Electrical Circuit from the Magnetic Device Physical Properties", *Texas Instruments*, pp. 1–7, 1994.
[35] A. Ducluzaux, "Extra losses caused in high current conductors by skin and proximity effects.", *Cahier Technique no 83 Schneider Electric*, pp. 1–22, 1983.
[36] R. Ridley, "Flyback Snubber Design", *Switching Power Magazine*, vol. 12, pp. 1–7, 2005.
[37] International Electrotechnical Commission, "CISPR 15:2013 – Limits and methods of measurement of radio disturbance characteristics of electrical lighting and similar equipment", IEC Standard, 2013.
[38] J. Amado, *Técnicas de Redução da Indutância de Dispersão em Indutores Acoplados e seu Impacto no Funcionamento de um Driver de LED Flyback Quase Ressonante*, Master's thesis, Universidade Federal de Santa Maria (UFSM), Santa Maria, RS, Brasil, 2025, available at: https://repositorio.ufsm.br/handle/1/34646.

BIOGRAPHIES

João Renato Camara Amado was born in Cruz Alta, Brazil, in 1996. He received the B.S. degree in Control and Automation Engineering from the Federal University of Santa Maria (UFSM), Santa Maria, Brazil, in 2021, and the M.Sc. degree in Electrical Engineering from UFSM in 2025. He is currently a Ph.D. candidate, also at UFSM. He has been a member of GEDRE – Intelligence in Lighting Group at UFSM since 2018 and has collaborated with Zagonel Iluminação S.A. since 2021. His work focuses on magnetic components and power density optimization for LED drivers. His research interests include power electronics applied to lighting systems, magnetic component design, and lighting products and applications.

Kalyl Sinhorini Abu Ali was born in Guaíra, Brazil, in 2003. He is currently pursuing a Bachelor's degree in Electrical Engineering at the Federal University of Santa Maria (UFSM). Since 2023, he has been a member of GEDRE – Intelligence in Lighting Group, at UFSM. His research involves finite element simulations applied to power electronics, including magnetic component modeling and analysis. His interests include power electronics and finite element analysis.

Giulia Kaufmann Grassi was born in Santa Maria, Brazil, in 2001. She received the B.S. degree in Electrical Engineering from the Federal University of Santa Maria (UFSM), Santa Maria, Brazil, in 2025. She is currently seeking the M.Sc. degree, also at the Federal University of Santa Maria. Since 2019, she has been a member of the GEDRE – Intelligence in Lighting Group, at UFSM. Her work has focused on high power density LED drivers and GaN semiconductors. Her main areas of interest are power electronic systems, LED drivers and artificial intelligence applied to lighting systems.

Hentony Amaral Lobo was born in the city of Rio Grande, in the state of Rio Grande do Sul, Brazil, in 2001. He received his technical degree in Electrotechnics in 2020 from the Technical College of Santa Maria (CTISM). He is currently pursuing a Bachelor's degree in Control and Automation Engineering at the Federal University of Santa Maria (UFSM). Since 2022, he has been a member of GEDRE – Intelligence in Lighting Group, at UFSM. His research involves inductor design, as well as the analysis of operation and control of converters. His interests include control of power electronic systems, artificial intelligence, and technological innovation in embedded systems design using artificial intelligence.

Renan Rodrigo Duarte received the B.S., M.Sc., and Ph.D. degrees in Electrical Engineering from the Federal University of Santa Maria (2015, 2017, and 2022, respectively). He completed a curricular internship at Fraunhofer IZM in Berlin, Germany, in the RF Smart Sensor Systems department (2014-2015) and worked as a senior designer at Zagonel S.A., focusing on hardware and embedded firmware design and development (2020-2023). Since 2023, he has been a professor at the Federal University of Santa Maria (UFSM). His main research areas include artificial lighting systems, high-efficiency converters, and GaN semiconductors.

Marco Antonio Dalla Costa (S'03, M'09, SM'17) received his B.S. and M.Sc. degrees in Electrical Engineering from the Federal University of Santa Maria, Brazil, in 2002 and 2004, respectively. He earned his Ph.D. degree (with honors) in Electrical Engineering from the University of Oviedo, Spain, in 2008. Since 2009, he has been serving as a Professor at the Federal University of Santa Maria, Brazil. Dr. Dalla Costa has co-authored over 240 journal and conference papers. His research interests include power electronics applied to lighting systems, LED drivers, LED modeling, horticultural lighting, and visible light communication systems. Since 2018, he has been serving as an Associate Editor for the IEEE Transactions on Industrial Electronics and the IEEE Journal of Emerging and Selected Topics in Power Electronics. Additionally, he chaired the IEEE Industry Applications Society's ILDC (2019–2020) and MSDAD (2020–2021).